Engineering Structures 175 (2018) 711–720

Contents lists available at ScienceDirect

Engineering Structures

journal homepage: www.elsevier.com/locate/engstruct

On the modeling and analysis of a vibration absorber for overhead powerlines with multiple resonant frequencies

N.K. Vaja[a], O.R. Barry[b,*], E.Y. Tanbour[c]

[a] Central Michigan University, Mt Pleasant, MI, USA
[b] Virginia Tech, Blackburg, VA, USA
[c] Eastern Michigan University, USA

ARTICLE INFO

Keywords:
Asymmetric Stockbridge damper
Aeolian vibration
Analytical model

ABSTRACT

Stockbridge dampers are primarily used to suppress or reduce Aeolian vibrations of transmission lines. The number of resonant frequencies characterizes the effectiveness of the Stockbridge damper. Aeolian vibrations refers to the vibration of conductor cables in the range of 3–150 Hz. Unlike the primitive Stockbridge damper which has only two resonant frequencies, the asymmetric Stockbridge damper exhibits up to four resonant frequencies. The numerical simulations and parametric studies conducted previously showed a correlation between the increase of natural frequencies and the change in the geometry of the counterweight. This paper presents an analytical model of a novel Aeolian vibration damper with an increased number of resonant frequencies. The analytical model is used to deduce the resonant frequencies of the damper. A 3D finite element model is developed to validate the analytical model. The natural frequencies and the subsequent mode shapes of both analytical and finite element models are presented. Experiment is conducted to validate the proposed models.

1. Introduction

Aeolian vibrations can cause fatigue and eventual failure of the transmission line. These are the most common kinds of vibrations observed in transmission lines and are caused by vortex shedding due to the laminar flow of wind. These low amplitude vibrations are characterized by frequencies between 3 and 150 Hz. The vibrations are noticed in the vertical plane, causing alternating bending stresses and eventual failure of the conductor cable. The catastrophic failure of the transmission line from Cowal junction to Longwood in London was due to Aeolian vibrations [1]. Several other recent incidents in Ontario and Manitoba were attributed to Aeolian vibrations [2,3]. I.F.Lazar et al., address this issue in their work on vibration suppression of cables [4].

The Stockbridge damper is one of the most common used dampers in controlling Aeolian vibrations. The conventional damper has two counter weights connected by a messenger cable. This assembly is hung from the conductor cable using an aluminum clamp. The absorption of energy is possible only if the natural frequencies of the damper are tuned to cover the range of Strouhal frequencies. The primitive Stockbridge damper developed by George H. Stockbridge in 1925, is termed as symmetric Stockbridge damper or 2R damper since the counter weights on both sides are symmetric, and the system possesses two resonant frequencies in the Strouhal frequency range [5]. The modern asymmetric Stockbridge damper or the 4R damper has unequal counterweights, and possesses four resonant frequencies [6]. Fig. 1 shows a commercially available asymmetric Stockbridge damper. It has unequal counter weights, and the length of the messenger cable on both sides is also unequal.

One of the leading concerns in designing new transmission lines is the efficiency of the Stockbridge damper. With a growing need for better dampers, design improvements have gained enormous attention [6]. Tuning the counterweights, length, and cross-section of the messenger cable can increase the number of resonant frequencies (i.e. natural frequencies falling within the range of the entire Strouhal frequency spectrum) of the Stockbridge damper, thus resulting in a significant performance improvement.

Numerous authors have developed mathematical models for asymmetric Stockbridge dampers [7–9]. Among them, the latest was developed by Barry et al., [10], in which the authors presented explicit expressions for the frequency equation and mode shapes of an asymmetric Stockbridge damper.

A common approach used by several researchers is to experimentally determine the natural frequencies from the impedance curve [11–23]. The technical preliminary considerations showcase two

* Corresponding author.
E-mail address: obarry@vt.edu (O.R. Barry).

https://doi.org/10.1016/j.engstruct.2018.08.051
Received 17 April 2017; Received in revised form 16 August 2018; Accepted 19 August 2018
Available online 01 September 2018
0141-0296/ Published by Elsevier Ltd.

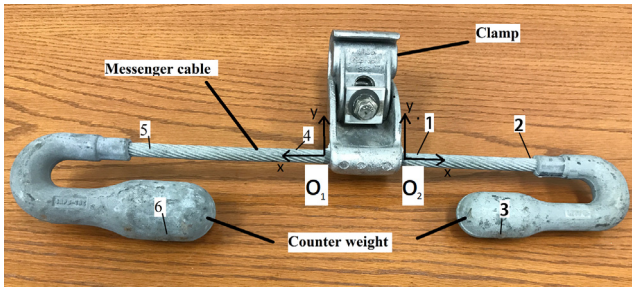

Fig. 1. Asymmetric Stockbridge damper.

methods of testing- the basic method and the direct method. The basic method is based on measuring the energy loss due to the damper, with the stockbridge damper attached to a test span of the cable. On the other hand, in the direct method, the stockbridge damper is directly mounted on an electro dynamic shaker, and only vertical excitation is imposed to determine the resonant frequencies [24,25]. The sources also mention that the basic method is desirable for an analysis of the whole system(cable and damper). The direct method is preferred to basic method out of technical and economic considerations. In the experiments conducted by Wanger et al., a constant displacement of 1 mm peak to peak was used with a frequency sweep between 2.5 and 35 Hz [26]. Lara-Lopex et al., also conducted similar experiments with a constant peak to peak displacement of 2.7 mm [27]. However, the measurement standards, as mentioned in requirements and tests for Stockbridge type aeolian vibration dampers (IEC 61 897) recommend testing the Stockbridge damper at a constant velocity [28].

This paper presents a novel vibration damper using analytical and finite element models. The messenger cable is modeled as a Euler-Bernoulli beam, and the cable is assumed to behave linearly. The governing equations of motion and boundary conditions are derived using Hamilton's principle. The frequency equation is obtained analytically and experiment is conducted to validate the proposed model. It is should be noted that the present work is an extension of the work by Vaja et al. [29].

2. Analytical model

A full scale solid model of the vibration damper is shown in Fig. 2.

The mathematical model of the whole Vibration damper will be enormous. To simplify the computation, a half model of the vibration damper is used. Fig. 3 shows the schematic of the half model of the vibration damper. Three coordinate systems(O_1, O_2, and O_3) are used. The model is treated as a three-beam and three-mass system. The first coordinate system O_1 is at the clamp with mass M_1 at the other end. The second and third coordinate systems are on either sides of the mass M_1, with mass M_2 and mass M_3 at their respective extreme ends. The mass M_1 is considered to have rotation about axis perpendicular to the length of messenger cable, while mass M_2 and M_3 are considered to be point masses. The vibration displacement along the j coordinate is given by

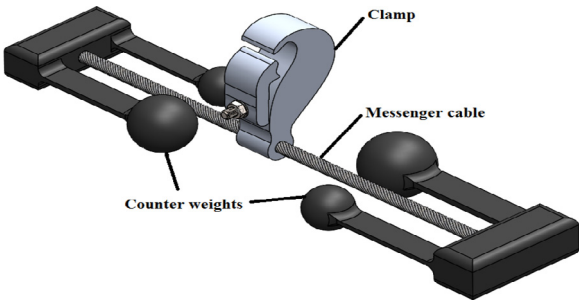

Fig. 2. Vibration damper.

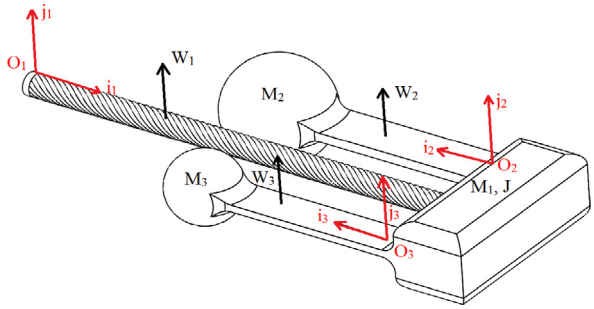

Fig. 3. Schematic of the quarter model of Vibration damper.

W_1, W_2 and W_3 respectively in the first, second and third coordinate systems.

The kinetic and potential energy of the system are given by Eqs. (1) and (2), respectively

$$T = \frac{1}{2}m_1\int_0^{L_1}\dot{W_1}^2(x_1,t)dx + \frac{1}{2}M_1\dot{W_1}^2(L_1,t) + \frac{1}{2}J\dot{W_1}'^2(L_1,t) + \frac{1}{2}m_2\int_0^{L_2}\dot{W_2}^2(x_2,t)dx + \frac{1}{2}M_2\dot{W_2}^2(L_2,t) + \frac{1}{2}m_3\int_0^{L_3}\dot{W_3}^2(x_3,t)dx + \frac{1}{2}M_3\dot{W_3}^2(L_3,t) \quad (1)$$

$$V = \frac{1}{2}EI_1\int_0^{L_1}W_1''^2(x_1,t)dx + \frac{1}{2}EI_2\int_0^{L_2}W_2''^2(x_2,t)dx + \frac{1}{2}EI_3\int_0^{L_3}W_3''^2(x_3,t)dx \quad (2)$$

The primes in the above equations represent differentiation with respect to x, and differentiation with respect to time is represented by dots. E is Youngs modulus, I_1, I_2 and I_3 are the area moment of inertia of the messenger cable and beams respectively. J is the rotational inertia of the mass M_1, L_1 is the length, and m_1 is the mass per unit length of the cable. L_2, L_3 are the lengths and m_2, m_3 are the mass per unit length of the beams respectively. Using Hamilton's principle, the equations of motion of the system are obtained as

$$EI_1W_1^{IV} + m_1\ddot{W_1} = 0 \quad (3)$$

$$EI_2W_2^{IV} + m_2\ddot{W_2} = 0 \quad (4)$$

$$EI_3W_3^{IV} + m_3\ddot{W_3} = 0 \quad (5)$$

Assuming the system exhibits harmonic motion, the following equations can be written

$$W_1(x_1,t) = F(x_1)e^{i\omega t} \quad (6)$$

$$W_2(x_2,t) = G(x_2)e^{i\omega t} \quad (7)$$

$$W_3(x_2,t) = H(x_3)e^{i\omega t} \quad (8)$$

where ω is the natural frequency and the mode shapes are given as

$$F(x_1) = a_1\sin\beta_1x_1 + a_2\cos\beta_1x_1 + a_3\sinh\beta_1x_1 + a_4\cosh\beta_1x_1 \quad (9)$$

$$G(x_2) = a_5\sin\beta_2x_2 + a_6\cos\beta_2x_2 + a_7\sinh\beta_2x_2 + a_8\cosh\beta_2x_2 \quad (10)$$

$$H(x_3) = a_9\sin\beta_3x_3 + a_{10}\cos\beta_3x_3 + a_{11}\sinh\beta_3x_3 + a_{12}\cosh\beta_3x_3 \quad (11)$$

Since the cable is fixed at the left end, the displacement and slope at this point are zero. Therefore the boundary conditions at $x_1 = 0$ are:

$$W_1(0,t) = 0; \quad (12)$$

$$W_1'(0,t) = 0; \quad (13)$$

At $x_1 = L_1$ the right end of the cable meets the mass M_1. At this point the displacement is assumed to be equal, but the slope is opposite in direction due to the choice of reference coordinate. Hence,

$$W_1(L_1, t) = W_2(0, t) = W_3(0, t); \quad (14)$$

$$W_1'(L_1, t) = -W_2'(0, t) = -W_3'(0, t); \quad (15)$$

The continuity conditions due to moment and shear at $x_1 = L_1$, $x_2 = 0$, and $x_3 = 0$ are:

$$EI_1 W_1''(L_1, t) - J\ddot{W}_1'(L_1, t) + EI_2 W_2''(0, t) + EI_3 W_3''(0, t) = 0; \quad (16)$$

$$-EI_1 W_1'''(L_1, t) - EI_2 W_2'''(0, t) - EI_3 W_3'''(0, t) = M_1 \ddot{W}_1(L_1, t); \quad (17)$$

The boundary conditions at $x_2 = L_2$ are:

$$W_2''(L_2, t) = 0; \quad (18)$$

$$M_2 \ddot{W}_2(L_2, t) - EI_2 W_2'''(L_2, t) = 0; \quad (19)$$

Similarly, the boundary conditions at $x_3 = L_3$ are:

$$W_3''(L_3, t) = 0; \quad (20)$$

$$M_3 \ddot{W}_3(L_3, t) - EI_3 W_3'''(L_3, t) = 0; \quad (21)$$

The characteristic equation is developed by subjecting the general solution to the above boundary conditions. Twelve simultaneous homogeneous equations are deduced and arranged to form the coefficient matrix shown in the appendix (Eq. (22)). The characteristic equation is obtained by equating the determinant of the coefficient matrix to zero.

3. Finite element modeling

A finite element model of the vibration damper is developed using SOLIDWORKS Simulation. Uniform material is applied to the whole system for calculation simplicity. The mesh parameters and material specifications of the finite element model are specified in Table 3. Fig. 8 shows the simplified CAD model and the meshed model of the vibration damper. The CAD model has a clamp in between the counterweights which has been replaced with fixed condition at the center. The green arrows indicate the fixing of translational and rotational degrees of freedom. Bonded type contact is defined as the contact condition for all faces in contact.

A model of the conventional Asymmetric Stockbridge damper is also developed, and the exact CAD model is meshed using curvature based meshing tool in SOLIDWORKS Simulation. No simplification has been made to the CAD model, since the results from the free vibration analysis will be validated against the experimental results. The left end of the half model of the Stockbridge damper is fixed, which implies that the body is restrained in three translational axes and three rotational axes. This boundary condition effectively models the clamp, which is fixed. Fig. 4 shows the meshed model of the asymmetric Stockbridge damper. The green arrows represent the constraints. A detailed view of the mesh is also shown in the figure. The mass of the large counter weight is 1.95 kg and its inertial tensor is given in Table 1. The mass of the small counter weight is 0.56 kg and its inertial tensor is given in Table 2. The mass per unit length of the messenger cable is 0.88 g/mm.

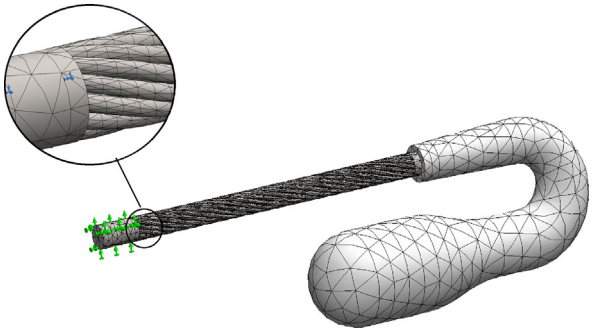

Fig. 4. Finite element model of the Stockbridge damper.

Table 1
Inertial tensor of the large counterweight in gmm^2

Jxx = 1179324.29	Jxy = 1625183.72	Jxz = −40.01
Jyx = 1625183.72	Jyy = 9684787.22	Jyz = −7.43
Jzx = −40.01	Jzy = −7.43	Jzz = 10420132.66

Table 2
Inertial tensor of the small counterweight in gmm^2

Jxx = 155541.75	Jxy = 279149.48	Jxz = −6.43
Jyx = 279149.48	Jyy = 1774671.82	Jyz = −1.12
Jzx = −6.43	Jzy = −1.12	Jzz = 1865948.58

Table 3
Mesh specifications and material properties of vibration damper

Mesh type	Solid curvature based mesh
Jacobian points	4 points
Max Element Size	7.09631 mm
Min Element Size	2.36541 mm
Total nodes	30345
Total elements	44.256
Maximum Aspect Ratio	40.332
Elements with Aspect Ratio < 3	98.7%
Elements with Aspect Ratio > 10	0.105%
% of distorted elements(Jacobian)	0
Material for messenger cable	ANSI 4130 Annealed Steel
Elastic Modulus	2.05e + 11 N/m^2
Poisson's Ratio	0.285
Mass Density	8000 kg/m^3
Material for counter weight	Cast steel
Elastic Modulus	6.61e + 11 N/m^2
Poisson's Ratio	0.27
Mass Density	7200 kg/m^3

The messenger cable is a standard 1x19 cable with one wire at the center and two layers wound around the core wire. The first layer has 6 helical strands,and the second layer has 12 helical strands. All the wires have uniform diameter of 2.44 mm. The radius of the first helical layer is 2.45 mm and the radius of the second helical layer is 4.9 mm with a uniform pitch of 96 mm for both (See Fig. 5).

Determining the natural frequencies for the models is the goal of this finite element analysis. SOLIDWORKS Simulation is used to effectively investigate the natural frequencies of both models. Since the moduli of elasticity of the materials used in the models are consistent, and the bonded type contact condition is used in the models, an FFE Plus solver is used. An improvement in the efficiency in situations with large degrees of freedom (> 100,000) is a characteristic feature of the FFE Plus solver. In an FFE Plus solver, iterative methods are used to solve the equations. In each iteration, a solution is assumed and the associated error is calculated. The iterations end when the solution has acceptable errors. Every resonant frequency is associated with a specific mode shape. An eigenvalue approach is used to determine mode shapes. The mode shapes of the vibration damper are shown in Figs. 13 and 14.

4. Experimental setup

The vibrations experienced by the damper on the cable comprise of translational movements along with rotational movements. In order to replicate the field vibrations in the laboratory, the Stockbridge damper has to be tested on a test span which is expensive. Also, the rotation experienced by the damper is very minimal, and can hence be neglected during experimentation. All the data obtained from testing the damper on the electrodynamic shaker was obtained only while imposing

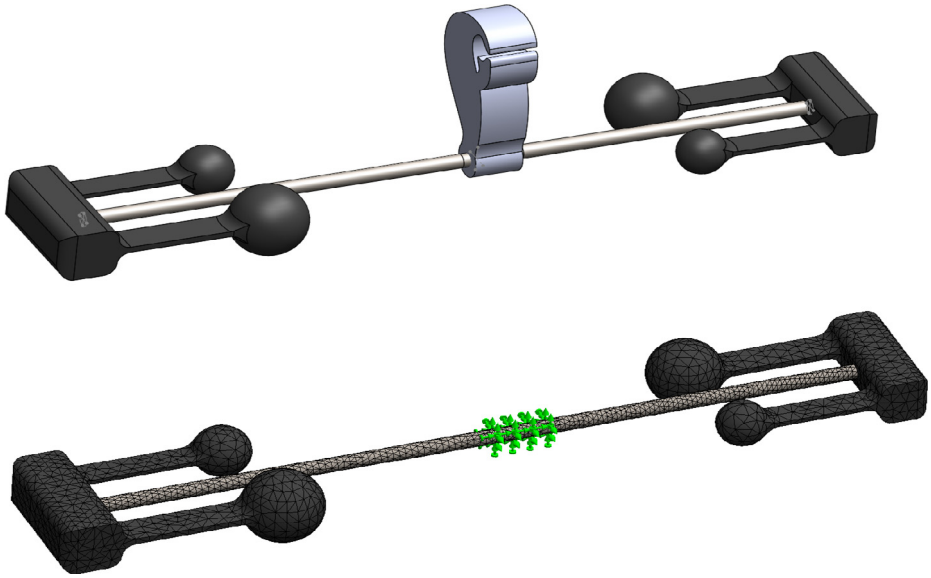

Fig. 5. Finite element model of the vibration damper.

vertical motion on the clamp following [28].

Fig. 6 shows the schematic representation of the experimental setup used in testing the asymmetric Stockbridge damper. A signal is generated by the controller (LASER USB,1.4 V) according to the profile programmed for the test. The signal from the controller is fed to the power amplifier (LSD SPA 16 K), where the signal is amplified, and a high voltage electric input is sent into the shaker. The movement of the shaker is recorded with the help of very light TEDs accelerometers (Bruel&Kjaer, Type 8325) placed on the head plate. The feedback signal is used by the controller to mitigate the error, and produce precise vibrations. A spectrum analyzer is also attached to the loop to capture the signals generated by the accelerometers, which are later used to generate acceleration and frequency graphs. A Bruel&Kjaer, V830-335-SPA16K electrodynamic shaker with a peak force of 2205 LBF and a frequency range of 5–3000 Hz was used for the experiment. The axial sensitivity of the accelerometers used was 10 mV/ms^{-2}, 5% with a peak measuring range of 750 m/s^2. The maximum output of the power amplifier used was 16 kVA, 480 Amps. Data from accelerometers was captured by the Bruel&Kjaer control systems software.

The asymmetric Stockbridge damper was rigidly mounted on the shaker head using a fixture, as shown in Fig. 7. The fixture is designed in a manner such that the transmissibility ratio for the shaker head to the top of the fixture remains close to one in the frequency range of 5 Hz–300 Hz. The clamp of the damper is attached to the top of the fixture. Accelerometer 1 was placed at the bottom of the fixture, and Accelerometer 2 was placed on the first counterweight to record the resonant frequencies. After completion, the accelerometer is switched to the other counterweight to record the second set of resonant frequencies. Using this technique, it is possible to obtain the measured data for both counterweights individually. Once the setup is in place, the electrodynamic shaker was oscillated in accordance with the IEC standard [28]. A sine sweep profile is programmed to run a frequency sweep from 5 Hz to 200 Hz with a constant velocity of 100 mm/s as recommended in [28]. The sweep is scheduled for an increment of 1 oct/min.

5. Results

The analytical model was used to determine the natural frequencies of the vibration damper. The finite element model served to validate the results from the analytical model. Table 4 shows the comparison between the natural frequencies obtained from both methods. The maximum difference was found to be 3.66%. Both models demonstrate that the new vibration damper exhibits six resonant frequencies in the Aeolian vibration frequency spectrum. This is a clear indication that the number of resonant frequencies has significantly improved in the novel vibration damper (six resonant frequencies), in comparison to the commercial Stockbridge damper (four resonant frequencies). It is also

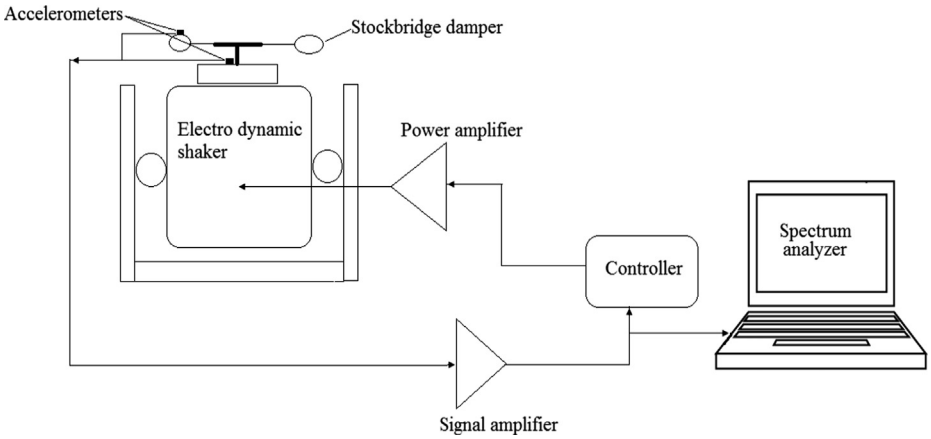

Fig. 6. Schematic of the experimental setup.

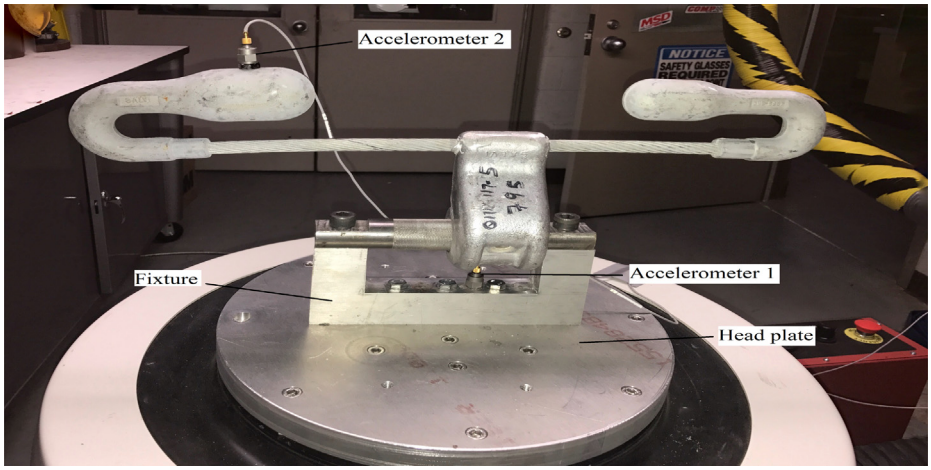

Fig. 7. Stockbridge damper mounted on the shaker.

Table 4
Natural frequency of numerical model and the analytical model of the Vibration damper

Mode	Numerical Model (Hz)	Analytical Model (Hz)
1	20.072	20.482
2	36.387	36.351
3	46.473	44.771
4	62.129	61.841
5	63.864	63.170
6	90.688	89.152

an indication of a 50% increased in the effectiveness of the damping capability.

Experiments were conducted to validate the accuracy of the numerical modeling technique. The conventional Stockbridge damper was used for this validation. As shown in the finite element modeling section, the numerical model of the conventional model was developed. Since the numerical model was validated against the experimental outcomes, it should be noted that the simplifications in the CAD model were kept to minimum and the contact conditions were accurately represented. An excitation frequency sweep was conducted for a range of 5–200 Hz with a logarithmic step size of 1 oct/min and the resonance frequency was collected from the experiments on the Stockbridge damper. The excitation was maintained at a constant velocity of 100 mm/s. The input excitation and the output response are both measured in terms of acceleration. The natural frequencies of the Stockbridge damper thus deduced from the numerical model and the experiments are presented in Table 5. A close correlation was observed in the results from both methods. The maximum error was 4.73%, which was acceptable.

Fig. 8 shows the frequency vs. non-dimensional transmissibility obtained from the experiments at constant velocity of 100 mm/s as recommended in [28]. The two curves shown in the plot represent the transmissibility of each counterweight. Each curve has two significant peaks, which represent the natural frequencies of the damper.

Table 5
Natural frequency of numerical model and the experiment on Stockbridge damper

Mode	Experimental natural frequency (Hz)	Numerical model natural frequency (Hz)	Error percentage
1	5.776	5.721	0.952
2	12.671	12.316	2.801
3	46.751	44.539	4.731
4	69.241	70.047	1.164

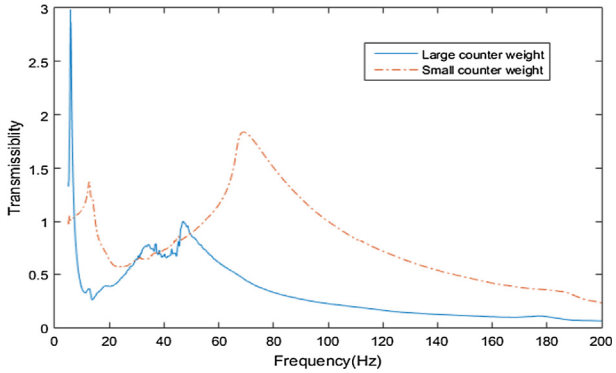

Fig. 8. Transmissibility plot of the free vibration analysis.

The effect of the excitation velocity on the experimental natural frequencies is depicted in Fig. 9. The velocity is varied from 60 mm/s to 120 mm/s. It can be observed that resonant frequencies of the Stockbridge damper decrease with increasing excitation velocity. This observation is consistent with both small and large counter weight as shown in Fig. 9(a) and (b), respectively. It should be noted, however, that the impact of the excitation velocity is more pronounced in the second natural frequency of the small counterweight. These findings corroborate those in the literature [8]. The changes in the obtained experimental resonant frequencies due to the variation of the excitation velocity are a clear indication that the dynamic behavior of Stockbridge dampers is nonlinear. However, the model presented in this paper does not account for any nonlinearity and hence the obtained analytical natural frequencies do not change with varying excitation velocity. To obtain a better representation of the dynamic of Stockbridge dampers, one should model the messenger cable using nonlinear curve beam theory with large displacement and rotation; thereby accounting for the frequency dependence on the vibration amplitude. This will be a subject for future work.

The last part of the experimental discussion is to examine how varying the output accelerometer location affects the resonant frequencies of the Stockbridge damper. As depicted in Fig. 1, six different locations of the output accelerometer (1, 2,3 4,5, and 6) are investigated. Considering O_1 and O_2 as origins the accelerometer positions 1,2,3 with respect to O_1 are at (5,5) (185,5) (180,61.97) and the accelerometer positions 4,5,6 with respect to O_2 are at (5,5) (190,5) (200,51.2), all dimensions are in mm. The center of gravity of the counterweights is shown in Figs. 10 and 11. The results are shown in Fig. 12 and indicate that the location of the output accelerometer has no effect on the first resonant frequencies of both larger and smaller

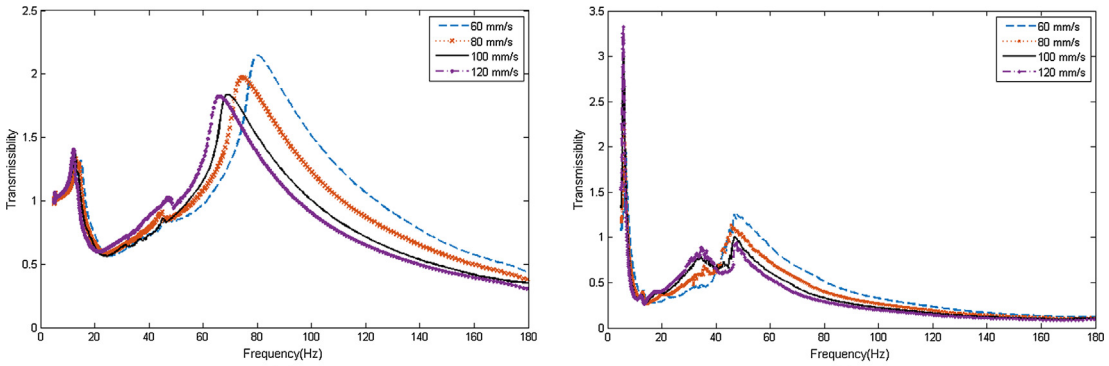

Fig. 9. Transmissibility plot with variation in excitation velocity.

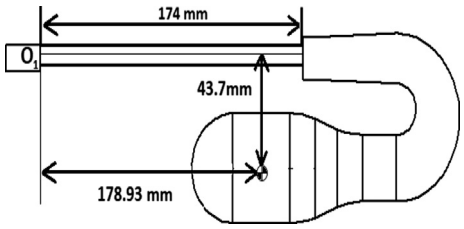

Fig. 10. Center of gravity of the small counterweight.

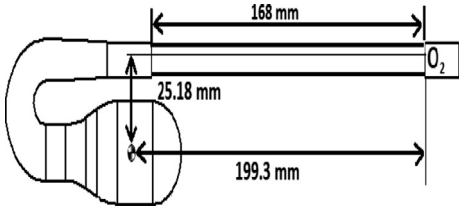

Fig. 11. Center of gravity of the large counterweight.

counterweights. However, the second resonant frequencies are affected by the location of the accelerometer. This effect is more pronounce for the smaller counterweight. Also, the vibration amplitude is significantly affected with varying the location of the output accelerometer. This is expected as the closer the accelerometer is to the clamp, the lower the vibration amplitude. The opposite is observed when the accelerometer is placed farther from the clamp; in that the output response is much higher. Fig. 10 also reveals that the top of the counterweight is the best location of the output accelerometer since the results for this case are in very good agreement with those of the analytical results.

6. Conclusion

The paper discusses about the need for improving the conventional Asymmetric Stockbridge damper. With previous investigations concluding that the change in counterweight design can lead to maximizing the resonant frequencies, a new vibration damper is designed. A mathematical model for the vibration damper is presented and the results from the analytical model are validated with the numerical model. The resonant frequencies of the Asymmetric damper is deduced using a numerical model and experiments. The results show a clear increase in the resonant frequencies with the new design, which is an indication of higher damping performance than the conventional Stockbridge damper. The geometric features of the novel vibration damper can be further tuned to achieve better damping and resonance characteristics. The authors anticipate that future work will focus on modeling the messenger cable using nonlinear curve beam theory in order to account for the frequency and vibration amplitude dependence.

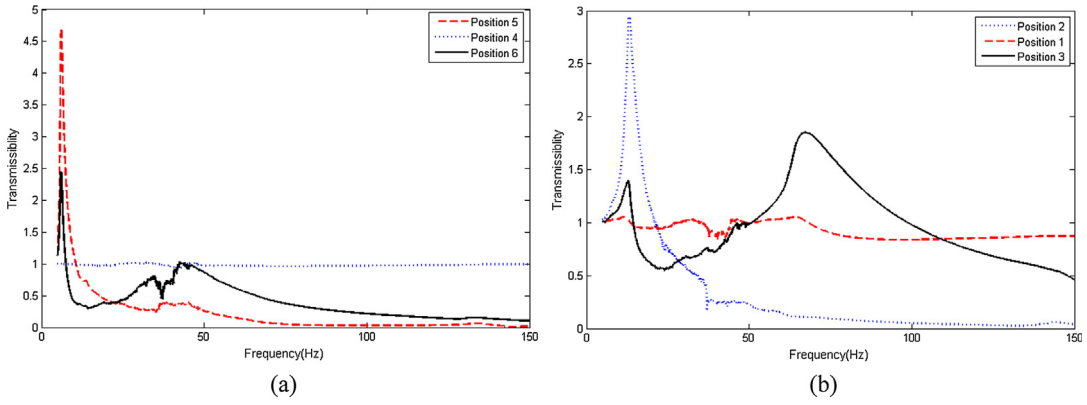

Fig. 12. Transmissibility plot with variation in output accelerometer location: (a) larger counterweight; (b) smaller counterweight.

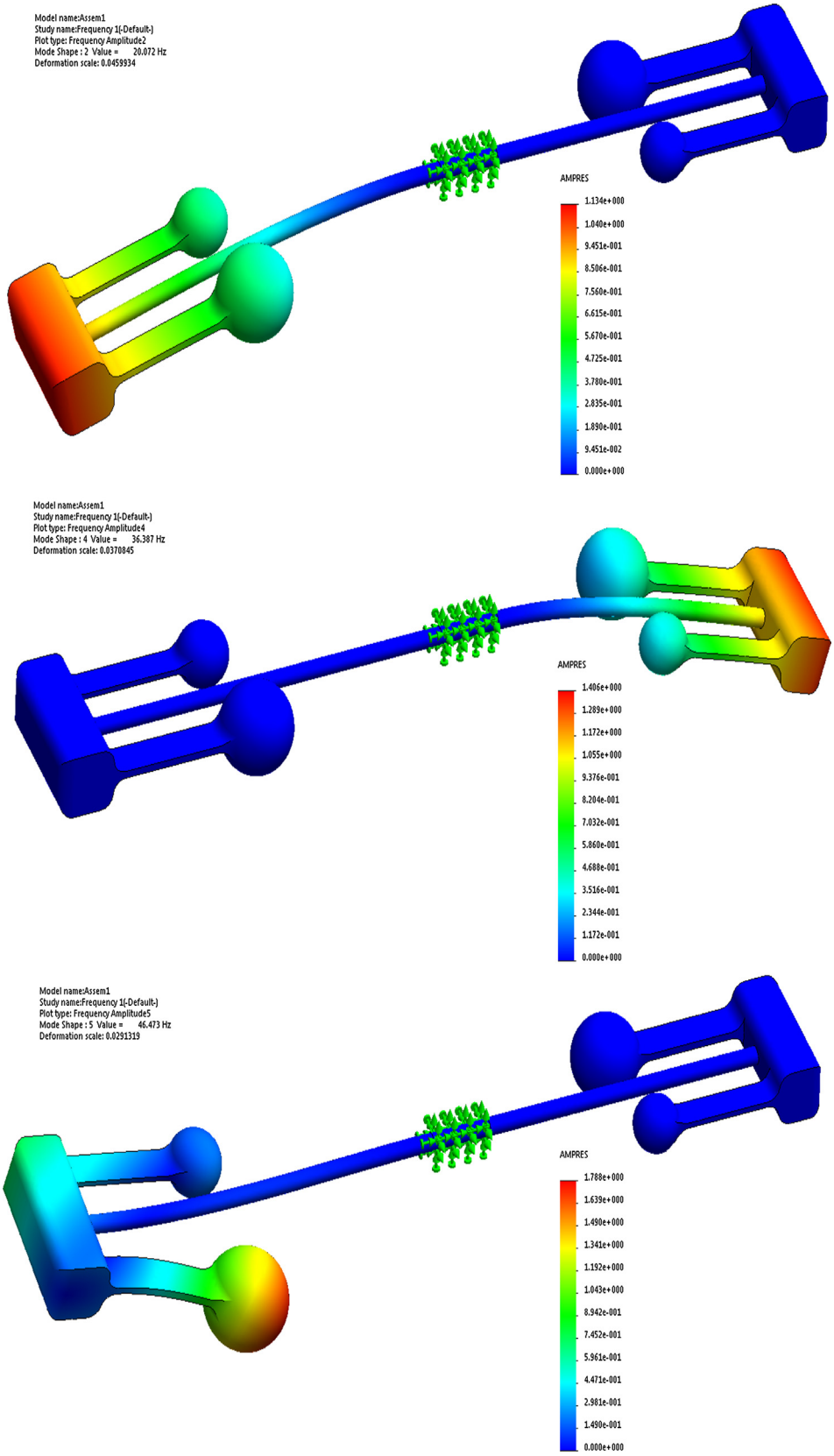

Fig. 13. Mode shapes corresponding to the first three natural frequencies of the Vibration damper.

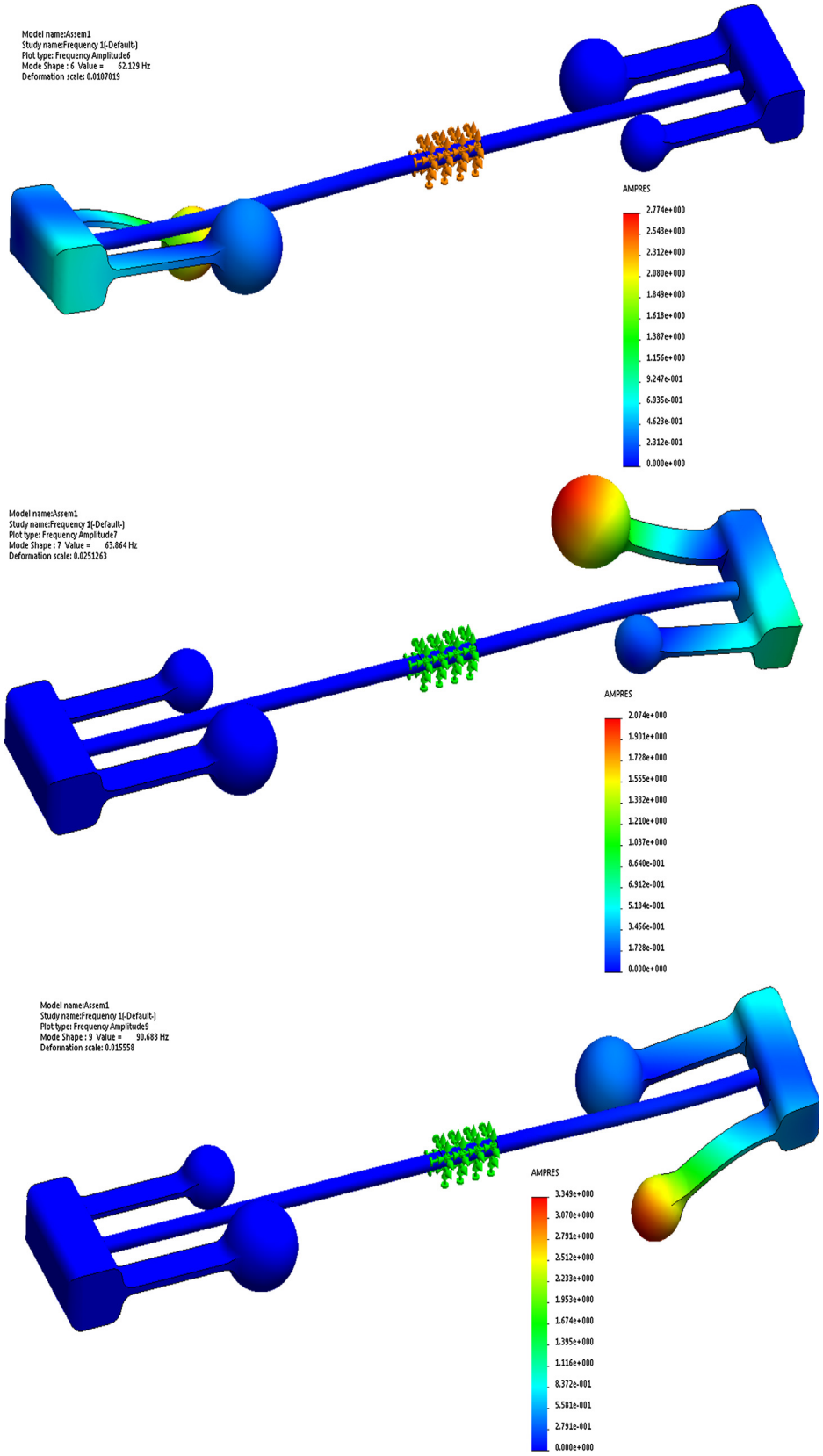

Fig. 14. Mode shapes corresponding to the fourth, fifth and sixth natural frequencies of the Vibration damper.

Appendix A

$$\begin{bmatrix} A_1 & 0 & A_3 & 0 & 0 & 0 & 0 & 0 & 0 & 0 & 0 & 0 \\ 0 & B_2 & 0 & B_4 & 0 & 0 & 0 & 0 & 0 & 0 & 0 & 0 \\ C_1 & C_2 & C_3 & C_4 & C_5 & 0 & C_7 & 0 & 0 & 0 & 0 & 0 \\ D_1 & D_2 & D_3 & D_4 & 0 & D_6 & 0 & D_8 & 0 & 0 & 0 & 0 \\ E_1 & E_2 & E_3 & E_4 & 0 & 0 & 0 & 0 & E_9 & 0 & E_{11} & 0 \\ F_1 & F_2 & F_3 & F_4 & 0 & 0 & 0 & 0 & 0 & F_{10} & 0 & F_{12} \\ G_1 & G_2 & G_3 & G_4 & G_5 & 0 & G_7 & 0 & G_9 & 0 & G_{11} & 0 \\ H_1 & H_2 & H_3 & H_4 & 0 & H_6 & 0 & H_8 & 0 & H_{10} & 0 & H_{12} \\ 0 & 0 & 0 & 0 & I_5 & I_6 & I_7 & I_8 & 0 & 0 & 0 & 0 \\ 0 & 0 & 0 & 0 & J_5 & J_6 & J_7 & J_8 & 0 & 0 & 0 & 0 \\ 0 & 0 & 0 & 0 & 0 & 0 & 0 & 0 & K_9 & K_{10} & K_{11} & K_{12} \\ 0 & 0 & 0 & 0 & 0 & 0 & 0 & 0 & L_9 & L_{10} & L_{11} & L_{12} \end{bmatrix} \cdot \begin{bmatrix} a_1 \\ a_2 \\ a_3 \\ a_4 \\ a_5 \\ a_6 \\ a_7 \\ a_8 \\ a_9 \\ a_{10} \\ a_{11} \\ a_{12} \end{bmatrix} = 0 \tag{22}$$

where

$A_1 = 1; \quad A_3 = 1$

$B_2 = -1; \quad B_4 = -1$

$C_1 = cos(\beta_1 L_1); \quad C_2 = sin(\beta_1 L_1);$
$C_3 = cosh(\beta_1 L_1); \quad C_4 = sinh(\beta_1 L_1);$
$C_5 = -1; \quad C_7 = -1$

$D_1 = -sin(\beta_1 L_1); \quad D_2 = cos(\beta_1 L_1);$
$D_3 = sinh(\beta_1 L_1); \quad D_4 = cosh(\beta_1 L_1);$
$D_6 = -\beta_2; \quad D_8 = -\beta_2$

$E_1 = cos(\beta_1 L_1); \quad E_2 = sin(\beta_1 L_1);$
$E_3 = cosh(\beta_1 L_1); \quad E_4 = sinh(\beta_1 L_1);$
$E_9 = -1; \quad E_{11} = -1$

$F_1 = -sin(\beta_1 L_1); \quad F_2 = cos(\beta_1 L_1);$
$F_3 = sinh(\beta_1 L_1); \quad F_4 = cosh(\beta_1 L_1);$
$F_6 = -\beta_3; \quad F_8 = -\beta_3$

$G_1 = \beta_1 J\omega^2 sin(\beta_1 L_1) - \beta_1^2 EI_1 cos(\beta_1 L_1); \quad G_2 = -\beta_1^2 EI_1 sin(\beta_1 L_1) - \beta_1 J\omega^2 cos(\beta_1 L_1);$
$G_3 = \beta_1^2 EI_1 cosh(\beta_1 L_1) - \beta_1 J\omega^2 sinh(\beta_1 L_1); \quad G_4 = \beta_1^2 EI_1 sinh(\beta_1 L_1) - \beta_1 J\omega^2 cosh(\beta_1 L_1);$
$G_5 = \beta_2^2 EI_2; \quad G_7 = \beta_2^2 EI_2;$
$G_9 = \beta_3^2 EI_3; \quad G_{11} = \beta_3^2 EI_3$

$H_1 = -\beta_1^3 EI_1 sin(\beta_1 L_1) + M_1\omega^2 cos(\beta_1 L_1); \quad H_2 = M_1\omega^2 sin(\beta_1 L_1) + \beta_1^3 EI_1 cos(\beta_1 L_1)$
$H_3 = -\beta_1^3 EI_1 sinh(\beta_1 L_1) + M_1\omega^2 cosh(\beta_1 L_1); \quad H_4 = -\beta_1^3 EI_1 cosh(\beta_1 L_1) + M_1\omega^2 sinh(\beta_1 L_1)$
$H_6 = \beta_2^3 EI_2; \quad H_8 = -\beta_2^3 EI_2$
$H_{10} = \beta_3^3 EI_3; \quad H_{12} = -\beta_3^3 EI_3$

$I_5 = -\beta_2^2 cos(\beta_2 L_2); \quad I_6 = -\beta_2^2 sin(\beta_2 L_2);$
$I_7 = \beta_2^2 cosh(\beta_2 L_2); \quad I_8 = \beta_2^2 sinh(\beta_2 L_2)$

$J_5 = \beta_2^3 EI_2 sin(\beta_2 L_2) + M_2\omega^2 cos(\beta_2 L_2); \quad J_6 = M_2\omega^2 sin(\beta_2 L_2) - \beta_2^3 EI_2 cos(\beta_2 L_2);$
$J_7 = \beta_2^3 EI_2 sinh(\beta_2 L_2) + M_2\omega^2 cosh(\beta_2 L_2); \quad J_8 = \beta_2^3 EI_2 cosh(\beta_2 L_2) + M_2\omega^2 sinh(\beta_2 L_2)$

$K_9 = -\beta_2^2 cos(\beta_2 L_2); \quad K_{10} = -\beta_2^2 sin(\beta_2 L_2);$
$K_{11} = \beta_2^2 cosh(\beta_2 L_2); \quad K_{12} = \beta_2^2 sinh(\beta_2 L_2)$

$L_9 = \beta_3^3 EI_3 sin(\beta_3 L_3) + M_3\omega^2 cos(\beta_3 L_3); \quad L_{10} = M_3\omega^2 sin(\beta_3 L_3) - \beta_3^3 EI_3 cos(\beta_3 L_3);$
$L_{11} = \beta_3^3 EI_3 sinh(\beta_3 L_3) + M_3\omega^2 cosh(\beta_3 L_3); \quad L_{12} = \beta_3^3 EI_3 cosh(\beta_3 L_3) + M_3\omega^2 sinh(\beta_3 L_3)$

References

[1] Havard D. Assessment of the Cowal JCT x Longwood TS for Vibration Control, Toronto, Ontario; 2008.
[2] McCarthy P, Melsness M. Severe Weather Elements Associated With September 5, 1996 Hydro Tower Failures Near Grosse Isle, Manitoba, Canada. Manitoba Environ Service Center Environ Can 1996;48(6):21.

[3] CIGRE Meeting. Conductor Motion, Toronto, Ontario; 2009.
[4] Lazar IF, Neild SA, Wagg DJ. Vibration suppression of cables using tuned inerter dampers. Eng Struct 2016;122(2016):62–71.
[5] Stockbridge G. Vibration Damper Patent No.1675391, USA Patent Office; 1925.
[6] Chan J. Transmission line reference book: wind-induced conductor motion. Palo Alto, CA: Electrical Power Research Institute; 2006.
[7] Burgreen D. Free vibrations of pin-ended column with constant distance between pin-ends. ASME J Appl Mech 1951;18:135139.
[8] Luo X, Wang L, Zhang Y. Nonlinear numerical model with contact for Stockbridge vibration damper and experimental validation. J Vib Control 2014;22(5):1217–27.
[9] Zhu ZH, Meguid SA. Nonlinear FE-based investigation of flexural damping of slacking wire cables. J Solids Structs 2006;44(2007):5122–33.
[10] Barry O, Zu JW, Oguamanam DCD. Nonlinear dynamics of stockbridge dampers. J Dyn Syst Meas Control 2015;137(6):061017.
[11] Lu MLC, Chan JK. An efficient algorithm for aeolian vibration of single conductor with multiple dampers. IEEE Trans Power Delivery 2007;22(3):18221829.
[12] Nigol O, Houston HJ. Aeolian vibration of single conductor and its control. IEEE Trans Power Delivery 1985;104(11):32453254.
[13] Kraus M, Hagedorn P. Aeolian vibration: wind energy input evaluated from measurements on an energized transmission lines. IEEE Trans Power Delivery 1991;6(3):12641270.
[14] Verma H, Hagedorn P. Wind induced vibration of long electrical overhead transmission line spans: a modified approach. J Wind Struct 2004;8(2):89106.
[15] Rawlins CB. Recent developments in conductor vibration. Alcoa Technical Paper No. 13; 1958.
[16] Vecchiarelly J, Curries IG, Havard DG. Computational analysis of aeolian conductor vibration with a stockbridge-type damper. J Fluids Struct 2000;14(4):489509.
[17] Havard DG. Weakness in the forced response method for testing vibration dampers. San Francisco, CA: Institute of Electrical and Electronics Engineers; 1994. p. 664.
[18] Claren R, Diana G. Mathematical analysis of transmission line vibration. IEEE Trans Power Delivery 1969;60(2):17411771.
[19] Diana G, Cigada A, Belloli M, Vanali M. Stokbridge type- damper effectiveness evaluation: Part 1. Comparison between tests on span and on the shaker. IEEE Trans Power Delivery 2003;18(4):14621469.
[20] Barry O, Oguamanam DCD, Lin DC. Aeolian vibration of a single conductor with a stockbridge damper. Proc Inst Mech Eng Part C 2013;227(5):935945.
[21] Barry O, Zu JW, Oguamanam DCD. Forced vibration of overhead transmission line: analytical and experimental investigation. ASME J Vib Acoust 2014;136(4):041012.
[22] Barry O, Zu JW, Oguamanam DCD. Forced vibration of overhead transmission line: analytical and experimental investigation. ASME J Vib Control 2014;136(4):041012.
[23] Barbieri N, Barbieri R. Dynamic analysis of stockbridge damper. Adv Acoust Vib 2012;2012(2012):659398.
[24] Guide on Conductor Self-Damping Measurements. IEEE Std. 5631978, May 26; 1978.
[25] Guide on the Measurement of the Performance of Aeolian Vibration Dampers for Single Conductors, IEEE Std. 6641993; 1993.
[26] Wagner H, Ramamurti V, Hartmann K. Dynamics of stockbridge damper. J Sound Vib 1973;30(2):207–20.
[27] Lara-Lopez A, Colin-Venegas J. Endurance of dampers for electric conductors. Int J Fatigue 2000;23:21–8.
[28] Requirements and tests for stockbridge type aeolian vibration dampers in IEC 61 897, Sept. 11; 1998.
[29] Vaja NK, Barry OR, Tanbour EY. On the dynamic modeling and analysis of an asymmetric Stockbridge damper. In: SEMC 2016: The 6th International conference on structural engineering, mechanics and computation Cape Town, South Africa. (September 5–7, 2016); 2016.